

NUMERICAL INVESTIGATION OF ELECTRICALLY EXCITED RTI USING ISPH METHOD

A. RAHMAT*[†], N. TOFIGHI* AND M. YILDIZ*

* Faculty of Engineering and Natural Sciences (FENS)
Sabanci University 34956
Istanbul, Turkey

[†]e-mail: arahmat@sabanciuniv.edu

Key words: Multi-Phase Flow, Interfacial Flow, Rayleigh-Taylor Instability, electrohydrodynamics, Smoothed Particle Hydrodynamics

Abstract. The influence of external electric field on the Rayleigh Taylor instability in a confined domain is numerically investigated using Smoothed Particle Hydrodynamics method. The leaky dielectric model is used for each of the flow phases having different electric permittivity and conductivities. The results are obtained for an Atwood number of 1/3 and gravitational Bond number of 100. It is shown that the electric force consists of two force components, namely the polarization force and electric field force. The polarization force acts in the direction of electric permittivity gradient of fluid phases at the vicinity of interface while the electric field force is influenced by the electric charge and electric field intensity. The role of electric force on the instability will be tested by adjusting the electric permittivity magnitudes of both fluid phases, keeping their ratio constant. The results will be presented for two permittivity ratios similar to those which have already been discussed.

1 INTRODUCTION

The Rayleigh-Taylor instability (RTI), the instable growth of two layers of fluid phases where a heavier bouyancy-associated fluid penetrates into a lighter one, was initially cited by Rayleigh [1] and Taylor [2]. The linear growth of the instability was analytically studied by Chandrashekar [3] and Mikaelian [4]. The long term investigations, however, have been carried out by Goncharov [5] and Abarzhi *et al.* [6], among others, to provide models for continuous bubble and spike evolutions from their earlier exponential growth to the nonlinear regime.

Electrically excited RTI has been the subject of many studies [7, 8, 9]. Raco [7] observed a direct relation between the intensity of the applied electric field and the behavior of the fluids. Later studies of Barannyk *et al.* [9] revealed that the instability may be controlled by the electrical properties and field intensities.

There have been several investigations of RTI within Smoothed Particle Hydrodynamics (SPH) framework [10, 11]. However, the combination of the two destabilizing agents, electric field and gravity, has not been fully investigated. In this study, the effect of presence of an external electric field on the evolution of RTI-like instability in a confined domain has been investigated numerically using Incompressible SPH (ISPH).

2 GOVERNING EQUATIONS

Evolution of velocity \mathbf{u} and pressure p fields of an incompressible, isothermal, two-phase, immiscible, viscous flow influenced by the presence of an external electric field may be formulated as

$$\nabla \cdot \mathbf{u} = 0, \quad (1)$$

$$\rho \frac{D\mathbf{u}}{Dt} = -\nabla p + \nabla \cdot (\mu (\nabla \mathbf{u} + \nabla \mathbf{u}^\dagger)) + \mathbf{f}_{(b)} + \mathbf{f}_{(s)} + \mathbf{f}_{(e)}, \quad (2)$$

where ρ and μ denote density and viscosity of the fluid. D/Dt is the material derivative defined as $\partial/\partial t + u^k \partial/\partial x^k$ where t and x^k denote time and spatial coordinate in k^{th} direction, respectively, while superscript \dagger denotes the transpose operation. Buoyancy is accounted for through $\mathbf{f}_{(b)} = \rho \mathbf{g}$ where \mathbf{g} is the gravitational acceleration.

Continuum Surface Force (CSF) method [12] is used to transform the local surface force into a local volumetric equivalent over a finite thickness, $\mathbf{f}_{(s)}$, employing a one-dimensional Dirac delta function, δ , as

$$\mathbf{f}_{(s)} = \gamma \kappa \hat{\mathbf{n}} \delta. \quad (3)$$

Here, surface tension coefficient, γ , is taken to be constant while κ represents interface curvature, $-\nabla \cdot \hat{\mathbf{n}}$, where $\hat{\mathbf{n}}$ is unit surface normal vector. In order to designate the interface and associate phase data, related thermodynamic properties and transport coefficients to different spatial locations, a color function \hat{c} is defined such that it assumes a value of zero for one phase and unity for the other.

Lorentz force, $\mathbf{f}_{(e)}$, also referred to as the resultant electric force throughout this work, exerted on the fluid due to the presence of an external electric field may be defined by taking the divergence of Maxwell stress tensor [13, 14],

$$\mathbf{f}_{(e)} = -\frac{1}{2} \mathbf{E} \cdot \mathbf{E} \nabla \varepsilon + q^v \mathbf{E} \quad (4)$$

Here ε and q^v denote electrical permittivity of the fluid and volume charge density, respectively, while \mathbf{E} represents the electric field vector. The first term on the right hand side, called the polarization force, will always act in a direction normal to the interface whereas the second term, a result of interactions between electric field and charged particles, is called electric field force.

3 NUMERICAL METHOD

Smoothed particle hydrodynamics (SPH) method is used to discretize the set of equations (1-4) over a set of finite spatial points called particles interacting through an interpolation kernel function. The kernel function $W(r_{ij}, h)$, concisely referred to as W_{ij} for a constant h , relates particle i and its neighboring particles j . Here, r_{ij} is the magnitude of distance vector $\mathbf{r}_{ij} = \mathbf{r}_i - \mathbf{r}_j$ while h is referred to as the smoothing length which controls the interaction length among particles. Among different kernel functions available in literature, quintic spline kernel [15] is chosen for its accuracy and robustness.

Such kernel function allows for any arbitrary variable f in a two dimensional domain Ω to be defined over a set of discrete points as

$$f(\mathbf{r}) \simeq \int_{\Omega} f(\mathbf{r}_j) W_{ij} d\mathbf{r}_j^2, \quad (5)$$

which upon replacing the integration with summation operation within the kernel function's support domain may be rewritten as

$$f(\mathbf{r}) \simeq \sum_j \frac{1}{\psi_j} f_j W_{ij}. \quad (6)$$

Here f_j denotes $f(\mathbf{r}_j)$ and the number density for particle i is defined as $\psi_i = \sum_j W_{ij}$. An alternate way of calculating the number density is to use particle density and mass as $\psi_i = \rho_i/m_i$, which sets ψ_i as a representative volume for particle i that will remain constant throughout the simulation for an incompressible flow.

Employing the Taylor series expansion in conjunction with the properties of the kernel function, first derivative and Laplace operators for vectorial and scalar quantities are approximated as

$$\frac{\partial f_i^m}{\partial x_i^k} a_i^{kl} = \sum_j \frac{1}{\psi_j} (f_j^m - f_i^m) \frac{\partial W_{ij}}{\partial x_i^l}, \quad (7)$$

$$\frac{\partial}{\partial x_i^k} \left(\varphi_i \frac{\partial f_i^m}{\partial x_i^k} \right) = 8[a_i^{ml}]^{-1} \sum_j \frac{2\varphi_i \varphi_j f_{ij}}{(\varphi_i + \varphi_j) \psi_j} \frac{r_{ij}^m}{r_{ij}^2} \frac{\partial W_{ij}}{\partial x_i^l}, \quad (8)$$

$$\frac{\partial}{\partial x_i^k} \left(\varphi_i \frac{\partial f_i^m}{\partial x_i^k} \right) = 8[2 + a_i^{kk}]^{-1} \sum_j \frac{2\varphi_i \varphi_j f_{ij}}{(\varphi_i + \varphi_j) \psi_j} \frac{r_{ij}^k}{r_{ij}^2} \frac{\partial W_{ij}}{\partial x_i^l}, \quad (9)$$

respectively. Here, f_{ij} denotes $(f_i - f_j)$ while $a_i^{ml} = \sum_j \frac{r_{ij}^m}{\psi_j} \frac{\partial W_{ij}}{\partial x_i^l}$ is a corrective second rank tensor which serves to eliminate particle inconsistencies arising from discrete form of the kernel function. Interested readers are referred to [16, 17] for more details.

4 SIMULATION PARAMETERS

Figure 1 provides a schematic view of the computational domain used during the simulations conducted in this study. A rectangle of height $h = 4$ and width $w = 1$ is discretized by 320×80 particles arranged in an equally spaced formation. Different phases are marked according to their positions relative to the interface coordinates, $x_{(s)}$ and $y_{(s)}$, defined as

$$y_{(s)} = 2 + \xi \cos(kx_{(s)}), \quad (10)$$

where particles above the interface are considered to belong to the heavier fluid marked by subscript h and those remaining underneath are assigned to the lighter one designated by subscript l . Disturbance amplitude, ξ , is taken to be 0.025 and the wave number k is equal to $2\pi/\lambda$ with λ taken equal to the width of the computational domain, w . During the simulations conducted in this study, heavier fluid penetrates the lighter one due to the presence of gravitational acceleration, g_o , pointing vertically downward.

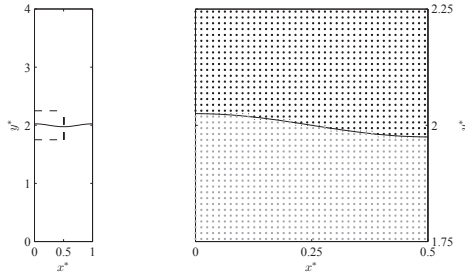


Figure 1: Initial condition used for simulations. (left) Whole domain; solid line shows the intended interface as defined in (10); heavy fluid on top, light fluid at the bottom. (right) Close up view of the portion included between the dashed lines on the right showing the initial particle positions in the vicinity of the interface. Solid line shows the intended interface profile while dashed line is the acquired interface profile calculated as 0.5 level contour of the color function.

Boundary conditions are applied through Multiple Boundary Tangent (MBT) [18] method where all bounding walls are assumed to abide the no-slip condition while a zero gradient condition is enforced for pressure. A uniform and steady electric field of magnitude $E_o = \Delta\phi/h$ pointing downward and parallel to side walls is generated by applying constant electric potential difference, $\Delta\phi$, to the horizontal plates.

Densities and viscosities of the fluid phases are assumed to be identical for all of the simulations carried out during this study. While both phases are assumed to have unit viscosity, a density ratio of 2 leads to an Atwood number of $At = (\rho_h - \rho_l) / (\rho_h + \rho_l) = 1/3$. Surface tension coefficient and gravitational acceleration's effects are combined in Bond number defined as

$$Bo = \frac{\rho_h g_o w^2}{\gamma} \quad (11)$$

Table 1: Simulation parameters for comparison of forces due to the applied electric field

Case	Bo	A_t	E_o (V/m)	ε_h (F/m)	ε_l (F/m)	σ_h (S/m)	σ_l (S/m)
A	100	0.33	1	0.5	1	150	50
B	100	0.33	1	1	0.5	50	150

while dimensionless time and positions are defined as

$$t^* = t\sqrt{g_o w}, \quad x^* = x/w, \quad y^* = y/w, \quad h_s^* = h_s/w, \quad h_b^* = h_b/w, \quad (12)$$

where h_s and h_b denote spike and bubble tip positions, respectively.

5 RESULTS

In this section, the results of the simulations are presented and discussed focusing on the competition among interfacial forces. The accuracy of the numerical method employed here has been tested out through multiple simulations which were carried out separately for Rayleigh-Taylor Like Instabilities [19] and two-phase flows involving an external electric field [16]. Consequently, such calculations have been left out for the sake of brevity.

5.1 The Comparison of Interfacial Forces

Figure 2 shows the comparison of interfacial forces for two cases having two different force configurations. In this figure, the arrows and filled contours respectively indicate the direction and the magnitude of the force vectors. The left column of figure 2 shows the forces corresponding the case at which the direction of the permittivity gradient vector is from the heavier fluid toward lighter fluid wherefore the electrical polarization force (the first term in equation (4)) points toward heavier fluid from the lighter one. As for the electric field force (the second term in equation (4)), it mainly acts from the heavier fluid into lighter one. The right column represents the inverse force configuration that can be achieved by enabling the permittivity gradient vector directed from the lighter fluid to heavier one, thereby resulting in the polarization and electric field forces to be in the opposite direction with respect to the case given in the left column. In this figure, the interface is shown for the dimensionless time of $t^* = 4.74$ at which the spike has started to have a mushroom like shaped front. Table 1 provides important simulation parameters for these two cases.

As it is apparent from equation (4), the electrical polarization force needs to be perpendicular to the interface while the orientation of the electric field force should be dependent on the interface profile and the direction of permittivity gradient vector as well as the applied electric field direction. For the cases shown in figure 2, the polarization force has greater magnitude on the frontier and main-stem of spike for case A and on the bubble frontier for case B. Similarly, the electric field force is concentrated on the spike tip for case A and on the bubble frontiers for case B. The comparison of magnitudes of the po-

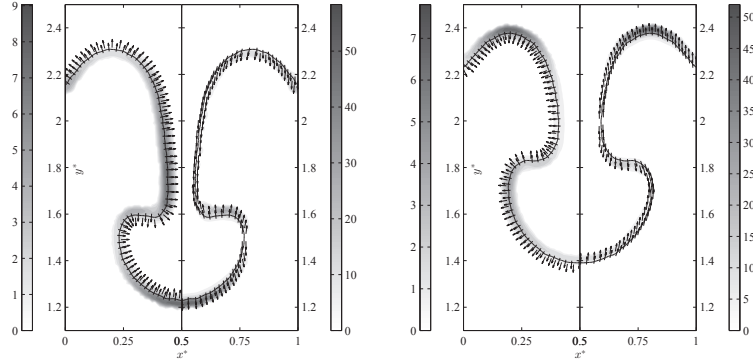


Figure 2: Comparison of components of the resultant electric force at $t^* = 4.74$; (left column) case A; (right column) case B. The left sub-column shows polarization forces while the right sub-column gives electric field forces. The direction and magnitude of the forces are respectively indicated by arrows and filled contour levels.

larization and electric field forces at the bubble and spike frontiers of both A and B cases clearly reveals that the electric field force is dominant over the polarization force on the tip positions of bubble and spike. On the other hand, the polarization force is obviously much greater than the electric field force on the stem of the spike where the interface is almost in the direction of applied electric field. Further observation of figure 2 for case A reveals that the electric field force tends to fasten the penetration of spike into the lighter fluid and slows down rise of the bubble into the heavier fluid. The polarization force affects the main stem by imposing an inward force to the heavier fluid from the lighter one, resulting in a narrow spike stem. As for the case B, the electric field force dominates the bubble and spike tip positions with the force direction opposite to that of case A, while the polarization force acts on the main stem area in such a way that it leads to thickening of main stem.

Figure 3 shows the comparison of the resultant electric force and the surface tension force. As the surface tension force is proportional to the interface curvature, equation 3, the surface tension force is concentrated at sharper corners. At this stage of instability, a surface tension force concentration is observed at spike saddle regions (where the stem and the mushroom head of the spike merge) and at the bubble tip positions. On the other hand, the resultant electrical force is dominant in bubble and spike tip positions where the electric field force is much greater in magnitude than the polarization force.

The left sub-column of figure 3 shows that the resultant electric force is much larger at the spike frontier in the growth direction of instability for case A. On the bubble frontier, the resultant electric force is in the downward direction thereby acting in way of hindering the rising motion of the bubble. The comparison of the resultant electric force and surface tension force reveals that at the spike frontier, forces are competitive whereby the effect of surface tension to form a circular topology is reduced. At the tip position of bubbles,

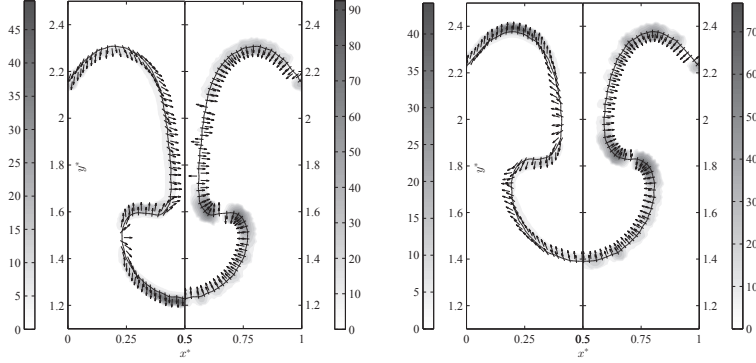


Figure 3: Comparison of the resultant electric force and surface tension force at $t^* = 4.74$; (left column) case A; (right column) case B. The left sub-column shows the resultant electric force while the right sub-column gives surface tension forces. The direction and magnitude of the forces are respectively indicated by arrows and filled contour levels.

both the resultant electric and surface tension forces are directed with respect to interface such as to impede the rising motion of the bubble. Wherever the interface is parallel to the electric field direction, the polarization force affects the interface in the transversal direction by exerting a force from the lighter fluid to the heavier one. Such an effect is especially observable at the spike stem where the surface tension is negligible as the curvature tends to zero. Another region at which the polarization force may be deemed effective is at well-developed side-tails of spike at later simulation times. In these regions, the polarization force has similarly a narrowing effect.

The right sub-column of figure 3 shows that the resultant electric force is prevailing in the bubble frontiers for case B. At the spike frontier, the resultant electric force is in a reverse direction with respect to the growth direction of the instability. This assists the surface tension force to generate a slower growth of the instability for the spike tip position. On the bubble frontier, however, the resultant electric force counters the surface tension force resulting in a faster rising bubble. The lateral polarization force tends to thicken the spike stem by providing an outward force from the spike to the lighter fluid. The polarization force may also help to widen the mushroom head in the lateral direction. As a result, the spike has a larger frontier which experiences a larger drag force from the lighter fluid.

5.2 Effect of Electric Permittivity Variations

As one of the influential parameters in the resultant electric force magnitude and direction in equation (4), the electric permittivity has a direct effect on the evolution of instabilities. Providing a better insight of this effect, additional test cases have been simulated by changing permittivity values whilst keeping their ratio constant.

Table 2: The comparison of various electric permittivity values

Case	Bo	A_t	E_o (V/m)	ε_h (F/m)	ε_l (F/m)	σ_h (S/m)	σ_l (S/m)
C-1	100	0.33	1	0.125	0.25	150	50
C-2	100	0.33	1	0.25	0.5	150	50
C-3	100	0.33	1	0.5	1	150	50
C-4	100	0.33	1	1	2	150	50
C-5	100	0.33	1	2	4	150	50
D-1	100	0.33	1	0.25	0.125	50	150
D-2	100	0.33	1	0.5	0.25	50	150
D-3	100	0.33	1	1	0.5	50	150
D-4	100	0.33	1	2	1	50	150
D-5	100	0.33	1	4	2	50	150

Table 2 presents the simulation parameters of simulation sets C and D. The simulation parameters of cases C-1 to C-5 bear resemblance to case A in terms of the direction of the electric permittivity gradient vector which is from the heavier fluid to lighter one. As for the opposite scenario which happens when the permittivity gradient vector is from lighter fluid to heavier one, the relevant test cases include C-1 to C-5. It should be noted that cases C-3 and D-3 of table 2 are identical to cases A and B of table 1, respectively.

Figure 4 shows a well-developed stage of instability at $h_s^* = 0.3$ for C series at top, and D series at the bottom row of the figure. An overview of sub-figures indicates that the increase in permittivity values leads to more contribution from the resultant electric forces on the growth of the instability. For instance, the comparison of upper and lower sub-figures of the first column of this figure 4 does not represent a considerable difference between two cases.

A detailed observation of C series indicates that the resultant electric forces have a considerable effect on the topology of side-tails and the position of the bubble. It is clear that as the value of electrical permittivity increases, the side-tails get thinner and smaller while the bubble rise gets slower due to the previously discussed reasons. It should be also noted that the amount of heavier fluid penetrating into the lighter one decreases due to the formation of a narrower jet of heavier fluid with small side-tails for simulations with higher electrical permittivity values such as cases C-4 and C-5.

The lower part of figure 4 shows that the electric permittivity increment enforces the side currents along the vertical walls to enclose the bubble and form a bubble entrapment. The side currents which are resulted from the lateral polarization force triggers the formation of secondary instabilities at the main stem, which are shown for the case D-3 (the third column of figure 4). The comparison of the bubble growth shows that there is a notable difference among the given test cases in terms of the bubble positions, shapes, and flow complexity, which is due to the highly influential effect of the resultant electric forces at the bubble tip position as elaborated in detail previously.

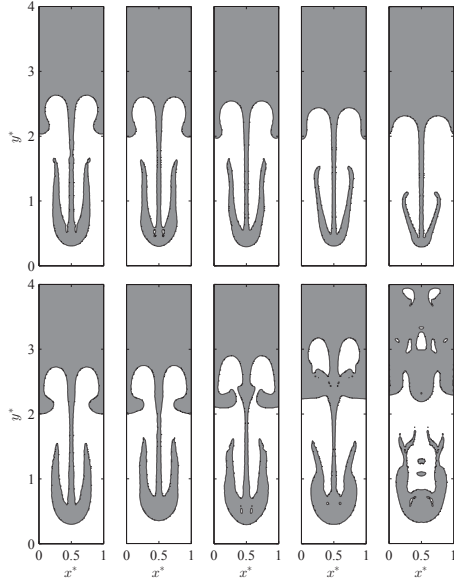


Figure 4: Snapshots of 0.5 level contour of color function at $h_s^* = 0.3$ for (top row) C series; (bottom row) D series. From left to right, snapshots correspond to case numbers 1 through 5 as set in table 2.

Figure 5 shows the bubble and spike tip positions versus time for three selected test cases (C-1, C-3, and C-5) of table 2 until the spike tip reaches at the final position of $h_s^* = 0.3$. As mentioned previously, the resultant electric forces enhance the penetration of spike into the lighter fluid while hindering the rising motion of the bubble for the C series test case. Intuitively, one may expect that the bubble front position for case C-5 should be the smallest among others because of the resultant electric force which acts to hinder the upward motion of the bubble. However, at earlier time steps, this is not the observed case due to the fact that the resultant electric force on the tip of the spike causes the spike to descend faster, thereby enabling the formation of strong hydrodynamics force due to the displacement of lighter fluid by the heavier one, which enhances the ascent of the bubble given that at early time steps, the bubble and spike tip positions are close to each other so that the motion of the spike can affect the bubble motion. A more detailed observation illustrates a turning point at dimensionless time around $t^* = 3.5$, after which this trend is reversed, meaning that the lower the electric permittivity, the higher the bubble position.

Similar to figure 5, figure 6 shows the bubble and spike tip positions for cases D-1, D-3 and D-5. In these cases, the resultant electric force is mainly dominant on the bubble tip position forming a faster rising bubble into the heavier fluid as the permittivity values increase. Figure 6 expresses that the spike tip positions of D series show a similar behavior to that of the bubble tip positions in C series. For D series, it is expected that the spike should descend slower in higher permittivity values due to the resisting nature of the

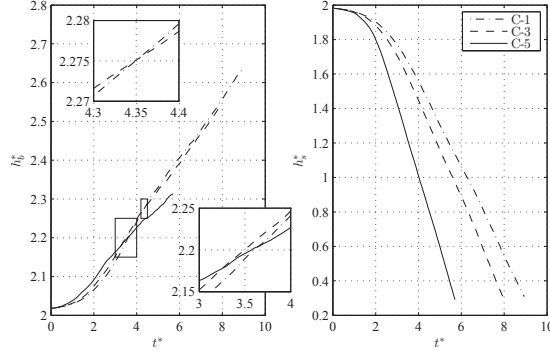


Figure 5: Bubble and spike tip positions for cases C-1, C-3, and C-5 of table 2 versus dimensionless time.

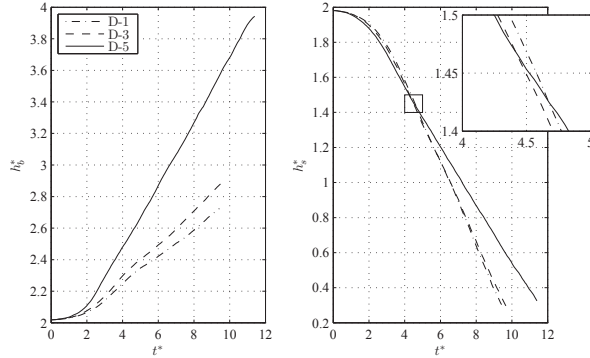


Figure 6: Bubble and spike tip positions for cases D-1, D-3, and D-5 of table 2 versus dimensionless time.

resultant electric forces at the frontier of the spike. However, it is observed that for higher permittivity values, the front of the spike grows faster at earlier time steps. The turning point is observed to be around $4 < t^* < 5$. The same justification, as given for C series, is valid for present observation. More specifically, the fast rising motion of bubble which is generated by greater resultant electric forces at its tip provides hydrodynamic forces to cause the spike to penetrate faster.

6 CONCLUSION

In this paper, the electrohydrodynamic evolution of wall-bounded Rayleigh-Taylor like instability is studied within the scope of Incompressible SPH. Considering relevant assumptions and using leaky dielectric model, the electric forces are obtained. The electric forces consist of two force components, namely the polarization force and the electric field force. The electric polarization force acts normal to the interface while the electric field

force is oriented in the direction of electric field. For both electric permittivity gradient cases, the polarization force is dominant wherever the interface is parallel to the instability growth direction, while the electric field force influence the instability mainly in bubble and spike front tips.

In order to observe electric force influence on the instability, the intensity of electric forces is varied by changing electric permittivity magnitudes. Increasing electric permittivity, it is observed that for the case having electric permittivity gradient from heavier to lighter fluid, despite having a resisting force at the bubble tips, the bubble rises faster at early time steps for higher electric force contributions. The spike tip provide forces in the direction of instability growth and enforce the bubble to penetrate in the heavier fluid. Similarly and for the other case, it is expected that due to the presence of resistive electric forces at the spike tip, the spike has a slower penetration in early times for larger electric force magnitudes. However, the electric forces at the bubble region enhance the rising motion of the bubble. This provides hydrodynamic forces exerted to the heavier fluid, resulting in faster penetration for larger electric force values at early time steps.

7 ACKNOWLEDGEMENTS

The authors gratefully acknowledge financial support provided by the Scientific and Technological Research Council of Turkey (TUBITAK) for the project 110M547 and the European Commission Research Directorate General under Marie Curie International Reintegration Grant program with the grant agreement number of PIRG03-GA-2008-231048.

References

- [1] Rayleigh, Investigation of the Character of the Equilibrium of an Incompressible Heavy Fluid of Variable Density, Proceedings of the London Mathematical Society s1-14 (1882) 170–177.
- [2] G. Taylor, The Instability of Liquid Surfaces when Accelerated in a Direction Perpendicular to their Planes. I, Proceedings of the Royal Society of London. Series A. Mathematical and Physical Sciences 201 (1950) 192–196.
- [3] S. Chandrashekar, Hydrodynamic and Hydromagnetic Stability, Dover Publications, New York, 1981.
- [4] K. Mikaelian, Effect of Viscosity on Rayleigh-Taylor and Richtmyer-Meshkov Instabilities, Physical Review E 47 (1993) 375–383.
- [5] V. Goncharov, Analytical Model of Nonlinear, Single-Mode, Classical Rayleigh-Taylor Instability at Arbitrary Atwood Numbers, Physical Review Letters 88 (2002).
- [6] S. Abarzhi, K. Nishihara, J. Glimm, Rayleigh-Taylor and Richtmyer-Meshkov Instabilities for Fluids with a Finite Density Ratio, Physics Letters A 317 (2003) 470–476.

- [7] R. J. Raco, Electrically Supported Column of Liquid, *Science* 160 (1968) 311–312.
- [8] A. E. M. A. Mohamed, E. S. F. E. Shehawy, Nonlinear Electrohydrodynamic Rayleigh-Taylor Instability. Part 1. A Perpendicular Field in the Absence of Surface Charges, *Journal of Fluid Mechanics* 129 (1983) 473–494.
- [9] L. L. Barannyk, D. T. Papageorgiou, P. G. Petropoulos, Suppression of Rayleigh-Taylor Instability Using Electric Fields, *Mathematics and Computers in Simulation* 82 (2012) 1008–1016. 6th IMACS International Conference on Nonlinear Evolution Equations and Wave Phenomena - Computation and Theory, Athens, GA, MAR 23-26, 2009.
- [10] A. Tartakovsky, P. Meakin, A Smoothed Particle Hydrodynamics Model for Miscible Flow in Three-Dimensional Fractures and the Two-Dimensional Rayleigh-Taylor Instability, *Journal of Computational Physics* 207 (2005) 610–624.
- [11] X. Y. Hu, N. A. Adams, An Incompressible Multi-Phase SPH Method, *Journal of Computational Physics* 227 (2007) 264–278.
- [12] J. Brackbill, D. Kothe, C. Zemach, A Continuum Method for Modeling Surface-Tension, *Journal of Computational Physics* 100 (1992) 335–354.
- [13] J. R. Melcher, G. I. Taylor, Electrohydrodynamics: A Review of the Role of Interfacial Shear Stresses, *Annual Review of Fluid Mechanics* 1 (1969) 111–146.
- [14] A. Eringen, G. Maugin, *Electrodynamics of Continua II: Fluids and Complex Media*, Springer London, Limited, 2011.
- [15] J. J. Monaghan, J. C. Lattanzio, A Refined Particle Method for Astrophysical Problems, *Astronomy & Astrophysics* 149 (1985) 135–143.
- [16] M. S. Shadloo, A. Rahmat, M. Yildiz, A Smoothed Particle Hydrodynamics Study on the Electrohydrodynamic Deformation of a Droplet Suspended in a Neutrally Buoyant Newtonian Fluid, *Computational Mechanics* 52 (2013) 693–707.
- [17] M. S. Shadloo, M. Yildiz, Numerical Modeling of Kelvin-Helmholtz Instability Using Smoothed Particle Hydrodynamics, *International Journal for Numerical Methods in Engineering* 87 (2011) 988–1006.
- [18] M. Yildiz, R. A. Rook, A. Suleman, SPH with the Multiple Boundary Tangent Method, *International Journal for Numerical Methods in Engineering* 77 (2009) 1416–1438.
- [19] M. S. Shadloo, A. Zainali, M. Yildiz, Simulation of Single Mode Rayleigh-Taylor Instability by SPH Method, *Computational Mechanics* 51 (2013) 699–715.